Baroclinic and Barotropic Instability Spectra as Functions of N in N-Level Models

D. O. STALEY

Department of Atmospheric Sciences, The University of Arizona, Tucson, AZ 85721

(Manuscript received 19 June 1985, in final form 21 February 1986)

ABSTRACT

The linear stabilities of simple baroclinic and barotropic flows are investigated by finite differencing of the quasi-geostrophic perturbation equations and reduction to the standard algebraic eigenproblem. In the baroclinic case, four different arrangements of winds and static stability are studied. In the barotropic case, cosine and hyperbolic secant jets are assumed between latitude walls. In all baroclinic and barotropic cases, only the number of levels is varied. In the baroclinic case, $2 \leq N \leq 26$. In the barotropic case, $3 \leq N \leq 20$, with solutions assumed to be symmetric across the wind maximum.

Increase of the number of levels, N, by one or a few does not assure a growth-rate spectrum closer to that for a great many levels. As N is increased from the minimum permissible number, the maximum growth rate, the corresponding phase velocity, and the wavelength of maximum growth rate, all describe irregular damped oscillations.

The results in the baroclinic cases depend greatly on the wind and temperature distributions. The two-level model may miss the existence of instability altogether, and in other cases small N may yield very poor descriptions of phase and amplitude, especially in the stratosphere and lower troposphere. Increase of N extends instability to shorter wavelengths, and secondary maxima varying with N are found at short wavelengths. In the barotropic case, small values of N may yield double maxima of similar strength at long wavelengths. For larger N, instability extends to shorter wavelengths, and a secondary maximum may appear at the shortwave end of the spectrum. The barotropic instability spectrum is very sensitive to subtleties of the wind distribution and shows large variations as truncation errors vary with changing N.

1. Introduction

The two-level model of Charney and Phillips (1953) and Phillips (1954) is widely recognized as providing a simple quantitative treatment of baroclinic instability suitable for introductory dynamical discussions (Holton, 1979). The frequencies for the normal mode solution to the perturbation equations are given by the two roots of a quadratic equation whose coefficients contain essential parameters of the undisturbed flow. These include one static stability parameter, $\sigma = -\alpha\partial \ln\theta/\partial p$, ostensibly evaluated at 500 mb, winds at the 750- and 250-mb levels, as well as wavelength, Coriolis and Rossby parameters. In such a simple model, any effects of vertical variations of static stability or shear cannot be investigated. Some of these effects were studied by Staley and Gall (1977), who found that baroclinic instability was increased and shifted to shorter wavelengths by small static stability and/or large vertical shear in the lower troposphere. It was also noted that merely the increase of levels, from two to four, shifted the instability to shorter wavelengths, provided the three static stability parameters are assigned the appropriate standard atmosphere values for their levels.

Multilevel models have also been used by Hirota (1968), Brown (1969), Simons (1972), Moen (1974), Simmons and Hoskins (1976) and Satyamurty et al. (1982). Moen shows the results of using 3, 5, 9 and 18 levels. The three-level case had levels at 300, 500 and 900 mb. The other three cases involved inserting intermediate levels, so that the number of levels was roughly doubled in each successive case. As boundary conditions, Moen used ψ = constant at $p = 0$ and $\omega \equiv dp/dt = 0$ at 950 mb. He found that a low vertical resolution is most serious when the horizontal (lateral) scale is small, and that high resolution models have a significantly higher instability in the short wave interval of 1000–2000 km.

Brown, Simons and Moen all found secondary maxima of instability at short wavelengths. Moen found a secondary maximum at 1300-km wavelength in a ten-level nongeostrophic model with constant static stability and vertical shear ($\partial U/\partial p$).

Satyamurty et al., in a study of subsynoptic-scale baroclinic instability with a Boussinesq primitive equation model, found that "inaccurate" results were obtained for wavelengths less than 2000 km with $\Delta z < 1.0$ km in a model with a lid at 10 km. They instead used 20 layers of 0.5 km thickness. For hyperbolic tangent profiles of wind and static stability, a veritable zoo of instability maxima was found between 600 and 5000 km, depending on static stability, shear, diabatic heating, and the sign of d^2U/dz^2.

Barotropic instability of simple jetlike flows can be studied with finite-difference models having as few as five "levels" in the north–south direction (Haltiner and

Song, 1962). For symmetric solutions only three levels are needed to detect the change of sign of the absolute vorticity gradient; a cubic frequency equation is obtained, with coefficients depending on Rossby parameter, wavelength and undisturbed winds. Aside from the obvious effect of reducing truncation error, it is not obvious what effect an increase of levels, beyond the minimum of three, would have on the predicted barotropic instability of a flow.

The previous studies indicate that the number of levels used has an effect on the instability spectra obtained. The effect is somewhat blurred by the variety of models and basic state parameters used, and also by gaps in the numbers of levels used. It appears that something can be learned by studying the effects, on computed barotropic and baroclinic linear instabilities, of varying systematically only the number of levels used. The purpose of this paper is to carry out such an investigation using the simplest quasi-geostrophic models applied to the simplest sorts of undisturbed flows.

2. Specifics of the algebraic eigenvalue problems

In the baroclinic case, the perturbation equation at the kth vertical level is

$$\left(\frac{\partial}{\partial t}+U_k\frac{\partial}{\partial_x}\right)\frac{\partial^2\psi_k}{\partial x^2}+\beta\frac{\partial\psi_k}{\partial x}-\delta_{k+1}\lambda_{k+1}^2$$
$$\times\left[\left(\frac{\partial}{\partial t}+\frac{U_k+U_{k+2}}{2}\frac{\partial}{\partial x}\right)\left(\psi_k-\psi_{k+2}\right)-\frac{1}{2}\left(U_k-U_{k+2}\right)\right.$$
$$\left.\times\frac{\partial}{\partial x}\left(\psi_k+\psi_{k+2}\right)\right]+\delta_{k-1}\lambda_{k-1}^2$$
$$\times\left[\left(\frac{\partial}{\partial t}+\frac{U_{k-2}+U_k}{2}\frac{\partial}{\partial x}\right)\left(\psi_{k-2}-\psi_k\right)\right.$$
$$\left.-\frac{1}{2}\left(U_{k-2}-U_k\right)\frac{\partial}{\partial x}\left(\psi_{k-2}+\psi_k\right)\right]=0. \quad (1)$$

Here t is time, x is distance toward the east, U is undisturbed zonal flow, ψ is streamfunction, β is the Rossby parameter, and

$$\lambda^2=\frac{f_0^2}{\sigma(\Delta p)^2} \quad (2)$$

where f_0 is a constant Coriolis parameter, $\sigma=-(\alpha/\theta)\times(\partial\theta/\partial p)$, and Δp is the pressure difference between successive odd levels. Also, in (1), $k=1, 3, 5, \cdots, 2N-1$, where N is the number of levels (matrix dimension); $\delta_2=\delta_4=\delta_6, \cdots, \delta_{2N-2}=1$; $\delta_0=\delta_{2N}=0$. The values of δ_0 and δ_{2N} reflect the boundary conditions $\omega=dp/dt=0$ at $p=0$, 1000 mb. The parameters f_0 and β are assumed to be 10^{-4} s^{-1} and 1.65×10^{-11} m^{-1} s^{-1}, respectively. Equation (1) is based on the baroclinic vorticity equation and thermodynamic energy equation and assumes perturbations independent of y. Physical details of the quasi-geostrophic model may be found, for example, in Holton (1979) or Staley and Gall (1977). When solutions are assumed in the form

$$\psi_k=\Psi_k e^{i\mu(x-ct)}, \quad (3)$$

where $\mu=2\pi/L$ and c is phase velocity, a system of N equations, homogeneous in Ψ_k are obtained, with c appearing linearly in certain coefficients. The system may be expressed as the standard algebraic eigenvalue problem:

$$(\mathbf{A}-c\mathbf{B})\Psi=0 \quad (4)$$

where $\mathbf{A}$ and $\mathbf{B}$ are tridiagonal $N\times N$ matrices. In baroclinic models, N is the number of odd-numbered levels interior to the $p=0$, 1000 mb levels.

In the problem of barotropic instability, the perturbation barotropic vorticity equation that will be solved here is

$$\left(\frac{\partial}{\partial t}+U\frac{\partial}{\partial x}\right)\nabla^2\psi+\left(\beta-\frac{d^2U}{dy^2}\right)\frac{\partial\psi}{\partial x}=0. \quad (5)$$

For solutions of the form

$$\psi=\Psi(y)e^{i\mu(x-ct)}, \quad (6)$$

Eq. (5) may be written for the jth lateral level as

$$(c-U)_j\left(\frac{d^2\Psi}{dy^2}-\mu^2\Psi\right)_j+(\beta-U_{yy})_j\Psi_j=0. \quad (7)$$

When $d^2\Psi/dy^2$ is expressed in finite difference form and the boundary conditions $\Psi_0=\Psi_N=0$ ($v=0$ at lateral boundaries) are applied, the standard eigenvalue problem (4) is again obtained. The matrices $\mathbf{A}$ and $\mathbf{B}$ are again tridiagonal.

In barotropic models, N is the number of levels internal to the boundaries, unless solutions symmetric about the center of the channel are assumed. In that case, N is half the number of internal levels plus one more.

The matrix elements can most efficiently be described by means of Tables 1 (baroclinic) and 2 (barotropic), in which the elements for specified diagonals are listed, proceeding down each diagonal from the upper left-hand end of the diagonal. In matrix $\mathbf{A}$ of Table 1, $c_R=U-\beta/\mu^2$. The values of U_{yy} appearing in matrix $\mathbf{A}$ of Table 2 were evaluated by finite differences to be consistent with the differencing of Ψ, although, for the prescribed jets, U_{yy} could have been evaluated analytically. Note that U on the boundaries must be specified for the evaluation by finite differences. In Table 2, d is the grid distance in the north–south direction. The factor of 2 at the lower ends of the lower diagonals is the consequence of assuming an undisturbed flow symmetric about the center of the channel and perturbations symmetric across the center.

3. Numerical results

The cases to be discussed in this section are described in Table 3.

TABLE 1. Nonzero matrix elements in the baroclinic case. Elements are listed starting with the first element at the upper left-hand corner of the matrix and ending in the lower right-hand corner.

Matrix **A** (asymmetric)			Matrix **B** (symmetric)	
Lower diagonal	Main diagonal	Upper diagonal	Lower = upper diagonal	Main diagonal
$\lambda_2^2 U_3$	$-(\mu^2 c_{R1} + \lambda_2^2 U_3)$	$\lambda_2^2 U_1$	λ_2^2	$-(\mu^2 + \lambda_2^2)$
$\lambda_4^2 U_5$	$-(\mu^2 c_{R3} + \lambda_4^2 U_5 + \lambda_2^2 U_1)$	$\lambda_4^2 U_3$	λ_4^2	$-(\mu^2 + \lambda_2^2 + \lambda_4^2)$
$\lambda_6^2 U_7$	$-(\mu^2 c_{R5} + \lambda_6^2 U_7 + \lambda_4^2 U_3)$	$\lambda_6^2 U_5$	λ_6^2	$-(\mu^2 + \lambda_4^2 + \lambda_6^2)$
.	.	.	.	.
.	.	.	.	.
.	.	.	.	.
.	.	.	.	.
$\lambda_{2N-2}^2 U_{2N-1}$	$-(\mu^2 c_{R2N-1} + \lambda_{2N-2}^2 U_{2N-3})$	$\lambda_{2N-2}^2 U_{2N-3}$	λ_{2N-2}^2	$-(\mu^2 + \lambda_{2N-2}^2)$

a. Baroclinic instability: winds linear and standard static stability

The undisturbed zonal wind was assumed to be zero at the surface and to increase linearly, with decrease of pressure, up to a maximum of 30 m s^{-1} at the tropopause (234 mb), and either remain constant above the tropopause or decrease linearly with p to zero at the top of the atmosphere. The difference of results between the two cases is small. For a tropopause above 250 mb, the two-level model is totally insensitive to the existence of a stratosphere.

For $N = 3$, the three levels are at 166.67, 500 and 833.33 mb, from which U_1, U_3 and U_5 are taken. Also used are λ_2 and λ_4 from the 333.33- and 666.67-mb levels.

For $N = 5$, the five levels are at 100, 300, 500, 700 and 900 mb, from which U_1, U_3, U_5, U_7 and U_9 are taken. Also used are λ_2, λ_4, λ_6 and λ_8 from the 200, 400, 600 and 800-mb levels.

Eigenvalues c were computed from (4) for each N as a function of wavelength. As with previous investigations, the largest instabilities were associated with wavelengths of a few thousand kilometers. For these wavelengths, one pair of complex conjugate eigenvalues was obtained when the undisturbed wind was constant at 30 m s^{-1} in the stratosphere, and a second pair, with a much smaller complex part, was obtained when wind decreased upward in the stratosphere. For wavelengths greater than about 7000 km, more than one pair of complex eigenvalues were occasionally found, but these were small and only the largest is mentioned here.

In Fig. 1, the maximum growth rate (MGR) and the wavelength of maximum instability of growth rate (WMI) are plotted as functions of N. The two-level model yields about half the MGR of models with larger N. The maximum is located at 5000 km, as compared to around 2900–3600 km for larger N. At least three levels are needed to approximate the results obtained for large values of N.

As N is increased to large values, the WMI resembles a damped oscillation, finally becoming essentially constant. The MGR continues to increase, although more and more slowly. The increase is probably related to

TABLE 2. Nonzero matrix elements in the barotropic case, assuming symmetric solutions. Elements are listed starting with the first element at the upper left-hand corner of the matrix and ending in the lower right-hand corner.

Matrix **A**			Matrix **B**		
Lower diagonal	Main diagonal	Upper diagonal	Lower diagonal	Main diagonal	Upper diagonal
U_2	$-\left[\left(\mu^2 + \frac{2}{d^2}\right)U_1 + U_{yy1} - \beta\right]$	U_1	1	$-(\mu^2 d^2 + 1)$	1
U_3	$-\left[\left(\mu^2 + \frac{2}{d^2}\right)U_2 + U_{yy2} - \beta\right]$	U_2	1	$-(\mu^2 d^2 + 1)$	1
U_4	$-\left[\left(\mu^2 + \frac{2}{d^2}\right)U_3 + U_{yy3} - \beta\right]$	U_3	⋮	⋮	⋮
⋮	⋮	⋮	⋮	⋮	⋮
$2\,U_N$	$-\left[\left(\mu^2 + \frac{2}{d^2}\right)U_N + U_{yyN} - \beta\right]$	U_{N-1}	2	$-(\mu^2 d^2 + 1)$	1

TABLE 3. Cases for which instability spectra were computed as functions of N. "Linear" denotes linear with respect to pressure, with different shear in troposphere and stratosphere. "Standard" denotes standard atmosphere with $\gamma = 6.5$ and 0 $K\,km^{-1}$ in the troposphere and stratosphere.

Case	Wind (U)	Static stability (σ)	Instability	Figures
a	linear	σ_{ST} at all levels	baroclinic	1–6
b	linear	$\gamma = 8.25\ K\,km^{-1}$ for $p > 800$ mb $\sigma = \sigma_{ST}$ for $p < 800$ mb	baroclinic	7–10
c	large shear in lower troposphere	σ_{ST} at all levels	baroclinic	11–13
d	large shear in upper troposphere	σ_{ST} at all levels	baroclinic	14–16
e	cosine and sech jets	—	barotropic	17–18

the selective effect of low-level static stability on baroclinic instability. With increase in N, smaller values of σ from closer to $p = 1000$ mb are brought into the growing **A** matrix. [Note $\sigma = c_n^2(\Gamma - \gamma)\gamma_a^{-1}p^{-2}$, where $c_n^2 = RT$; Γ, γ and γ_a are adiabatic, environmental and autoconvective lapse rates, respectively; and R is the gas constant.] For $N = 10$, the lowest level at which stability is used is 900 mb; for $N = 20$, the lowest level is 950 mb. This suggests that the growth rate for an infinite number of levels (or an analytic solution) might be estimated by adding to the growth rate for $N = 20$ the growth rate increment from $N = 10$ to 20. This increment is of the order of 10^{-2} d^{-1}.

The dashed curves in Fig. 1 are MGR and WMI when the wind decreases linearly to zero in the stratosphere. The negative shear thus reduces L_x by essentially a constant amount for $N > 2$, but the growth rate is affected only for $N = 3$.

Figure 1 also depicts the variation of phase velocity corresponding to the WMI. The phase velocity decreases rapidly as N is increased from two, but the percentage change is smaller than those of the WMI and the growth rate. The decrease as N increases from 2 to 20 is only about 15%.

Figure 2 depicts growth-rate spectra of baroclinic instability for $N = 2$, 3, 4, 5, 6, 10, 20 and 26. Since the growth-rate spectra are not sharply peaked, the WMI shown in Fig. 1 is primarily a way of characterizing the general shift of the growth-rate curves, but it is not a good predictor of observed wavelengths.

The two-level model can be partly rehabilitated by tuning with the stability factor. In the $N = 2$ case in Fig. 2 are shown the results of using one-half and one-third the standard atmosphere σ at 500 mb. The WMI

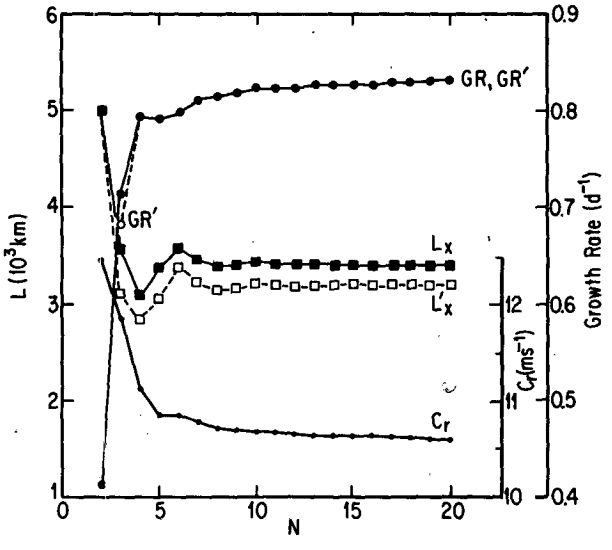

FIG. 1. Case a. Maximum growth rate (GR) and wavelength (L_x) of maximum growth rate and corresponding phase velocity (C_r) for baroclinic instability as functions of N. Solid curves are for winds constant in the stratosphere. Curves labeled with primed quantities are for winds decreasing in the stratosphere.

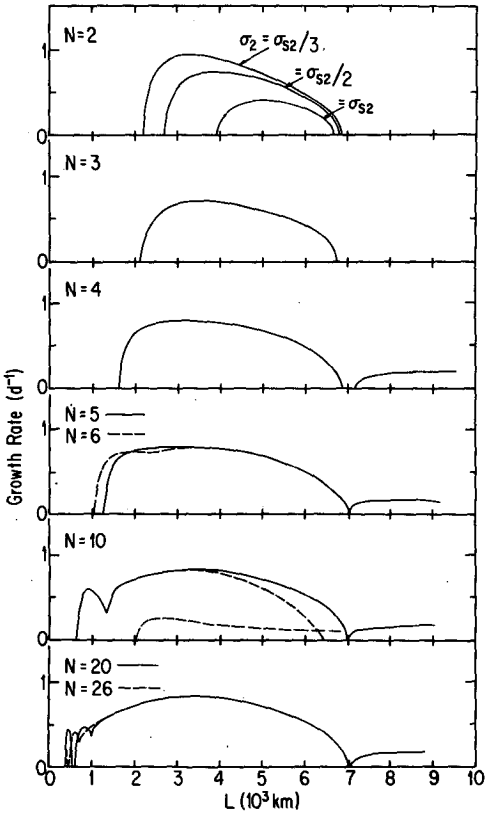

FIG. 2. Case a. Growth-rate spectra for baroclinic instability as functions of wavelength for various N. Dashed curves for $N = 10$ are for winds decreasing in the stratosphere.

and the critical wavelength at the short wavelength end of the spectrum are both reduced. However, the physical justification for substantially smaller σ is not obvious. If σ is averaged over the pressure depth of the troposphere of the standard atmosphere, the average turns out to be very near the value for 500 mb, or about 0.03 $m^2\ s^{-2}\ mb^{-2}$, implying $\lambda^2 \approx 1.3 \times 10^{-12}$ m^{-2} for $f_0 = 10^{-4}\ s^{-1}$. It is interesting to note that the version of the two-level quasi-geostrophic model formulated by Lorenz (1960) has a static stability parameter with effectively half the value of that in Phillip's model (Hollingsworth, 1975).

Since the two-level model leads to a quadratic equation which can be solved for eigenvalues, it is possible to derive analytic expressions for critical shear and critical wavelength necessary for instability (Holton, 1979):

$$U(250) - U(750) > \frac{\beta}{\lambda_2^2}, \quad L_c > \sqrt{2}\pi/\lambda_2.$$

For quantitative estimates of critical shear and wavelength, these expressions are obviously extremely inaccurate. The latter expression, for example, yields 3900 km for the critical wavelengths. Only proportionalities to β and static stability can be believed.

Figure 2 shows that the ultralongwave (Green mode) instability for $L \gtrsim 7000$ km appears only for $N \gtrsim 4$.

The effect of letting undisturbed U decrease linearly to zero from its maximum at the tropopause (30 m s^{-1} at 234 mb) is shown for the case $N = 10$. The instability for $L \gtrsim 4000$ km is reduced, and an additional slower amplifying mode is introduced with MGR around 2600 km.

For $N = 6$, an additional peak appears in the growth-rate spectrum at 1900 km. As N is increased, this peak shifts systematically to shorter wavelengths, as shown by the lower curve in Fig. 3, which depicts wavelengths of peak instability as functions of N. For $N = 14$, a third peak appears at 1150 km. Again, as N is increased, this peak shifts to shorter wavelengths. Thus, as N is increased, additional maxima appear at short wavelengths and move as ripples toward still shorter wavelengths. Since the geostrophic model must for various reasons, including diffusion (MacVean, 1983), be unrealistic at sufficiently short wavelengths, the lower curve in Fig. 3 was terminated for $N = 21$. The growth rates of these additional peaks range from 0.75 down to 0.45 d^{-1}. Generally, as N is increased further, the spectrum smooths to shorter and shorter wavelengths, and the peaks appear at shorter and shorter wavelengths. Since these short waves are confined to the lower troposphere, resolution can be increased by putting the upper boundary condition ($\omega = 0$) at a level below the top of the atmosphere. For $\omega = 0$ at $p = 500$ mb, the resolution for $N = 26$ is doubled below 500 compared to the previous case for $N = 26$. The spectrum was smoothed, compared to the previous case, in the range 400 to 800 km, and instability was extended down to 250 km.

The quasi-geostrophic model is, of course, not justified at these short wavelengths. However, the quasi-geostrophic terms would be present in more realistic ageostrophic models and not abruptly lost at any wavelength as wavelength is decreased. Hence the shifting maxima related to N noted here may not be eliminated by using physically more realistic models.

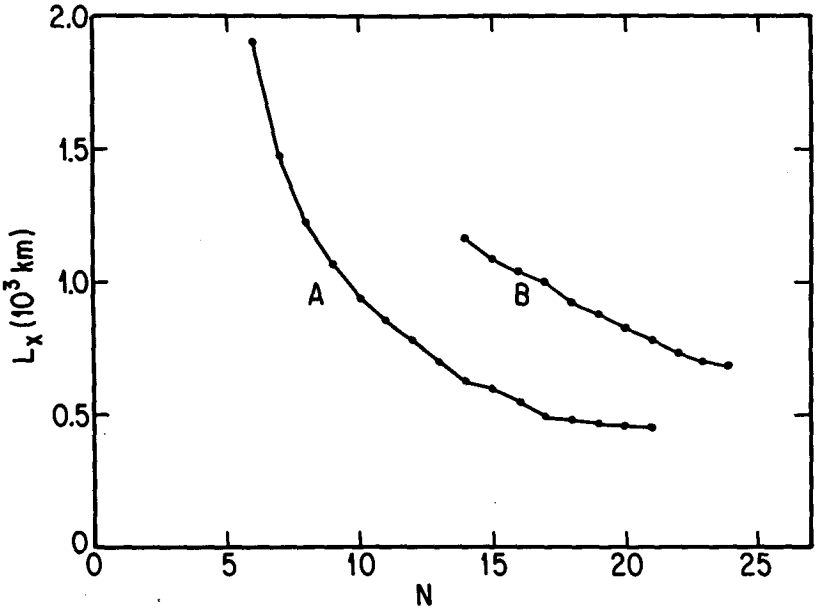

FIG. 3. Case a. Wavelengths of (A) second and (B) third peaks of baroclinic instability, as functions of N.

Figure 4 depicts amplitudes and phases of ψ and ω for smaller values of N. The scales for the various amplitudes in Fig. 4a are individually arbitrary; the horizontal positions are arbitrary so that the curves are separated. It is understood that $\omega = 0$ for all N at $p = 0$, 1000 mb. In all cases, the WMI was used. The pressure of maximum ω is located at p = 500, 667, 500 and 600 mb for N = 2, 3, 4 and 5, respectively (as determined from the unsmoothed curves.) These curves and pressures may be compared with the ω amplitudes in Fig. 5a for larger values of N. For $N = 20$, the maximum of ω is clearly seen to occur around 660 mb.

The streamfunction amplitudes in Fig. 4a for $N < 5$ do not give accurate indications of the amplitude profile for $N = 20$ in Fig. 5a.

Phases of ψ and ω are depicted in Fig. 4b. For all N, the streamfunction (eigenvector) at the highest level was arbitrarily given the complex value $\Psi = \Psi_r + i\Psi_i = 1$. Thus the phase of ψ at the uppermost point for all N is 360°. (The phase and amplitudes of ψ at all other levels follow from this specification of Ψ. The amplitude and phase of ω follow from the thermodynamic energy equation by setting $\omega = \Omega \exp[i\mu \times (x - ct)]$, where $\Omega = \Omega_r + i\Omega_i$.) The computed phase angles are given on the abscissa of Figs. 4b and 5b. To assist the interpretation, a scale of fractional wavelengths is also shown, with values increasing to the left. With this scale, the view is from the north looking south, with west to the right and east to the left. Thus constant phase lines of ψ slope up to the west. The corresponding phase lines of ω are displaced roughly $L/4$ to the east and also slope up to the west.

Differences in the phase curves in Figs. 4b and 5b, where they cover common pressure ranges, are due partly to the condition that phase of ψ at the uppermost level (which varies with N) be 360°. However, at 500 mb, the phase of ω leads (is downstream of) the corresponding phase of ψ by approximately 100°, 120°, 80°, 110° and 110° for N = 2, 3, 4, 5 and 20, respectively.

Figure 5b shows that for large N the phase of ω gradually increases its lead over the corresponding phase of ψ with increasing height in the lower troposphere, ranging from about 70° at 975 mb up to 110° at 500 mb. The maximum of ω is thus found between the ridge and the downstream trough over this pressure range. At 975 mb, $\omega < 0$ at the trough, while at 500 mb, $\omega > 0$ at the trough. These features are depicted more specifically in Fig. 6.

Figure 5b also shows that the phase of ω, when well resolved with a large N, shifts rapidly above the tropopause to a much greater lead over the corresponding

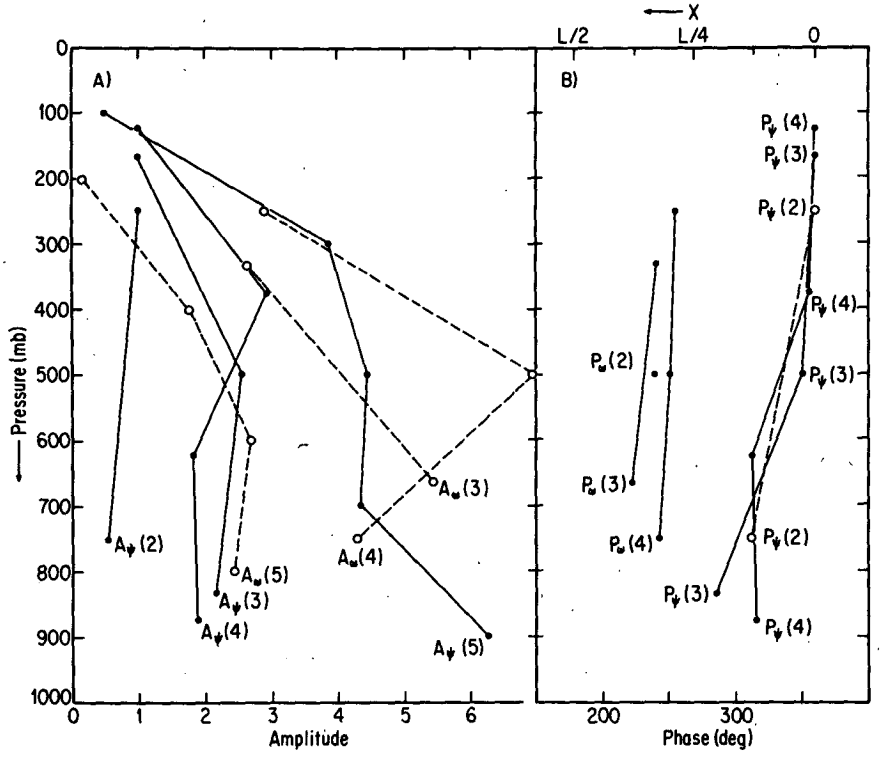

FIG. 4. Case a. Amplitude and phase of streamfunction (ψ) and $dp/dt(\omega)$ as functions of height for various N. Units for amplitude in (a) are arbitrary for each N and chosen to separate curves horizontally. Phases of ψ in (b) were arbitrarily set equal to 360° at the highest level for each N. The phase is alternatively expressed at the top of (b) as fractions of a wavelength (L).

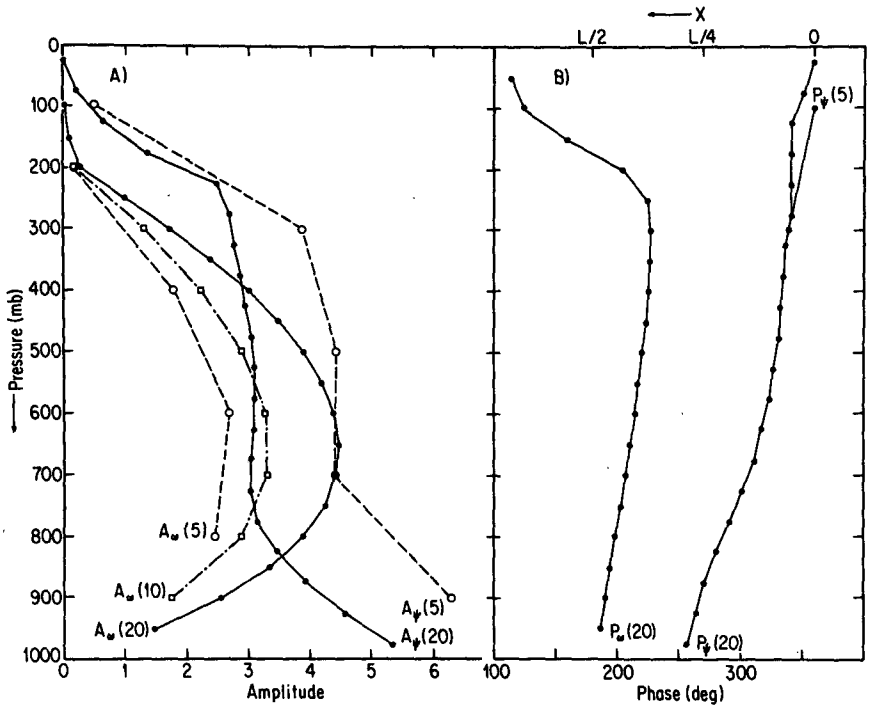

FIG. 5. Case a. As in Fig. 4 but for larger N.

phase of ψ. At 100 mb, maximum ω is found between the trough and the downstream ridge, as depicted in Fig. 6. Of course, the amplitudes of ψ and ω both attenuate rapidly upward above the tropopause.

b. Baroclinic instability: winds linear, $\gamma = 8.25$ K km^{-1} for $p > 800$ mb and $\sigma = \sigma_{ST}$ standard for $p < 800$ mb

It is known that low static stability in the lower troposphere shifts maximum instability to short wavelengths and increases the baroclinic growth rates. In this case, we examine the N-level model's perception of low static stability in the lower troposphere as N is increased.

Figure 7 depicts the WMI and the corresponding MGR and phase velocity as functions of N. For $N \leqslant 5$, all are similar to those in case a, where the static stability was standard at all levels. The minor differences are the result of letting the wind decrease in the stratosphere in the present case. The reason for the similarity is simply that the lower static stability is not perceived until $N = 6$. For $N = 5$, the lowest level at which static stability enters the computation is at 800 mb, while for $N = 6$ the static stability at 833 mb is used.

The effect of using $N \geqslant 6$ is dramatic. The WMI is shifted downward to 1000 km or less. The phase velocity also decreases dramatically, by 50% between $N = 5$ and 10. The growth rate increases on the order of 50%. It may be noted that the WMI and corresponding phase velocity for $N \geqslant 6$ show periodic gradual decreases followed by abrupt increases. The abrupt increases occur when an additional level, where static stability is used, drops below 800 mb. This occurs when N changes from 10 to 11, from 15 to 16, and from 20 to 21. Each time a new low stability level is added, it appears just below 800 mb, lifting the mean level of low static stability and increasing the WMI. In between the addition of a new level below 800 mb, the original levels sink, thereby decreasing the WMI.

The MGR again shows, as in Fig. 1, a gradual increase as N is increased, and smaller and smaller static stability parameters near the lower boundary are used.

Figure 8 depicts growth-rate spectra for $N = 5$, 6, 10, 11 and 20. The dramatic decrease of the WMI that occurs between $N = 5$ and 6 (Fig. 7) corresponds to an abrupt bulging up of the spectrum at shorter wavelength. For some values of N, a secondary maximum remains around 3000 km. When a new level for stability is added below 800 mb, as at $N = 6$, 11 and 16 (not shown), the secondary maximum is suppressed.

Figure 9a depicts the vertical distributions of the amplitudes of the streamfunction and vertical velocity for $N = 5$, 6, in each case for the WMI. The change from $N = 5$ to 6 drastically lowers the level of maximum vertical velocity and makes the streamfunction attenuate much more rapidly upward. This is consistent with the perception for $N = 6$ (but not for $N = 5$) of small static stability at the lowest model static stability level.

The phase differences between streamfunction and vertical velocity in Fig. 9b are similar for $N = 5$ and

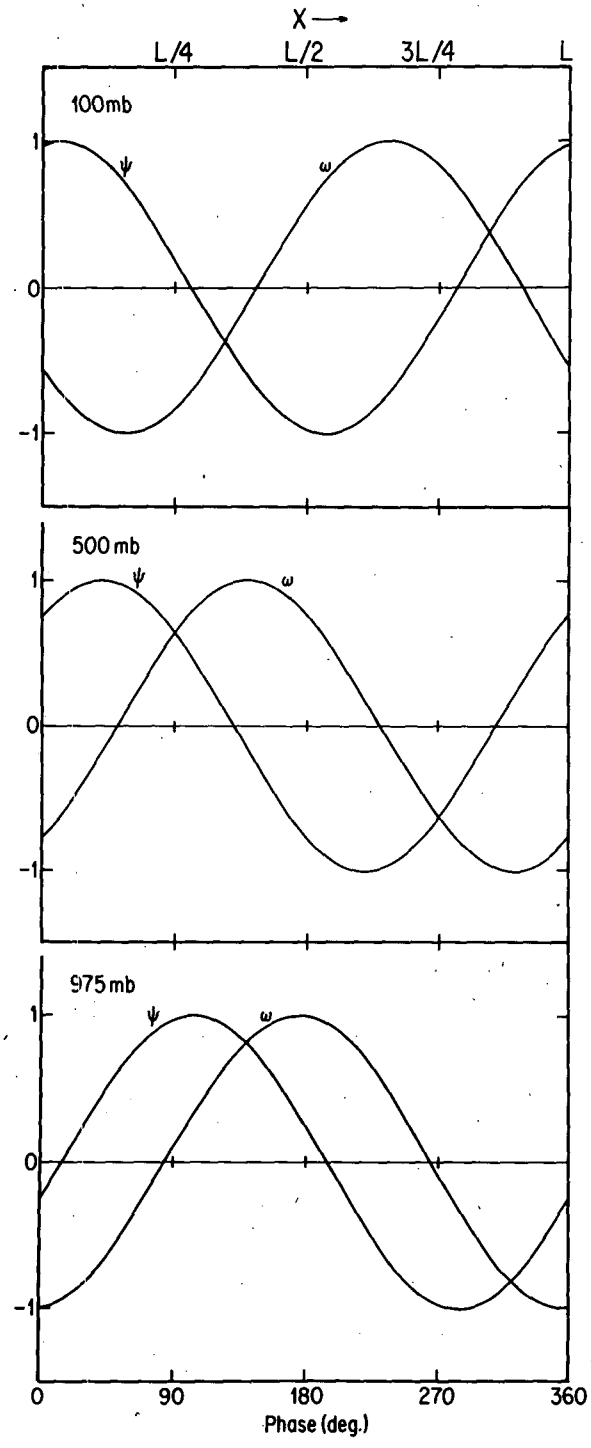

FIG. 6. Case a. Relative positions (phases) of ψ and ω perturbations at 975, 500 and 100 mb in terms of degrees (bottom scale) and wavelength fraction (top scale). Amplitude arbitrarily set equal to unity for all curves.

6. However, the phase difference between ψ and ω for $N = 6$ decreases somewhat with height between 750 and 350 mb, whereas for $N = 5$ the phase difference only increases with height.

Figure 10a depicts amplitude distributions of ψ and ω for $N = 10$ and 20. The principal feature of interest is the perception for $N = 20$ of a maximum of ω at 850 mb, whereas for $N = 10$ the maximum is found at or below 900 mb, the lowest model level for which ω is computed.

Figure 10b depicts vertical phase distributions of ψ and ω for $N = 10$, 20. There is little difference except that for $N = 20$ the rapid increase of phase difference in the stratosphere is much better resolved, as in Fig. 5b.

c. *Baroclinic instability: large shear in the lower troposphere and standard atmosphere at all levels*

In this case, the wind in the troposphere ($p \geq 234$ mb) is described by

$$U = \frac{U_T}{766}(1000 - p) + 10 \sin[\pi(1000 - p)/766], \quad (8)$$

where $U_T = 30$ m s^{-1} and p in mb yields U in m s^{-1}. This U differs from that of the previous two cases by the addition of the second term. This term vanishes for $p = 1000$ and 234 mb, is positive in-between, and places maximum shear at $p = 1000$ mb.

Figure 11 depicts the WMI and the corresponding MGR. For $N = 2$, no instability is found. The reason is that the shear between 750 and 250 mb, which enters the two-level model, is greatly reduced by the presence of the second term in (8). The shear becomes subcritical. Instability first appears for $N = 3$, and as N in-

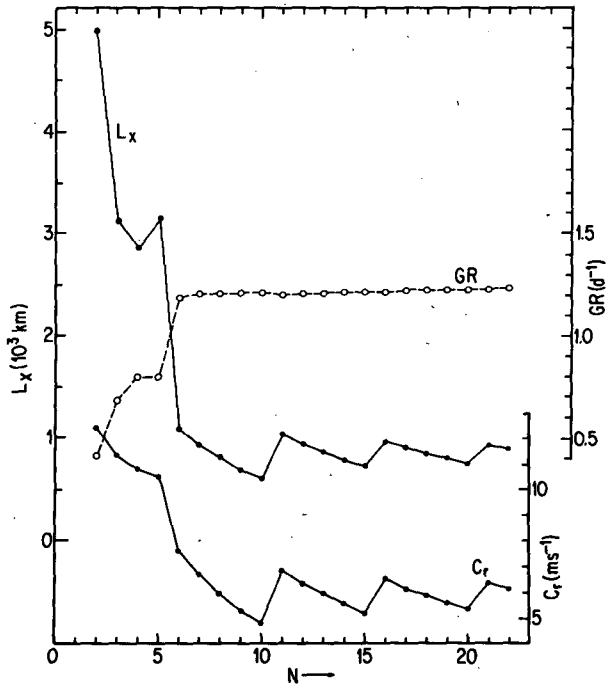

FIG. 7. As in Fig. 1 but for case b.

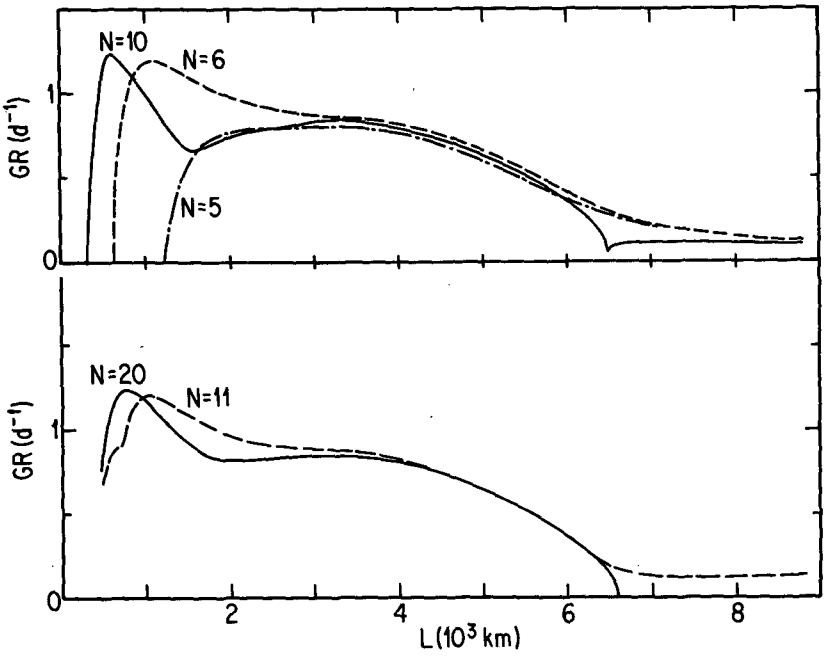

FIG. 8. As in Fig. 2 but for case b. Wind maximum always at tropopause.

creases, the WMI decreases sharply. For $N = 3$, the L_x is 2900 km but decreases to 1100 km at $N = 9$, at which N a new maximum appears around 2000 km. As N is increased further, the latter L_x resembles a damped oscillation. These features are qualitatively similar to those of Fig. 1, but the final L_x for large N is shorter and the final growth rate is larger, as would be expected from the large baroclinity at low levels.

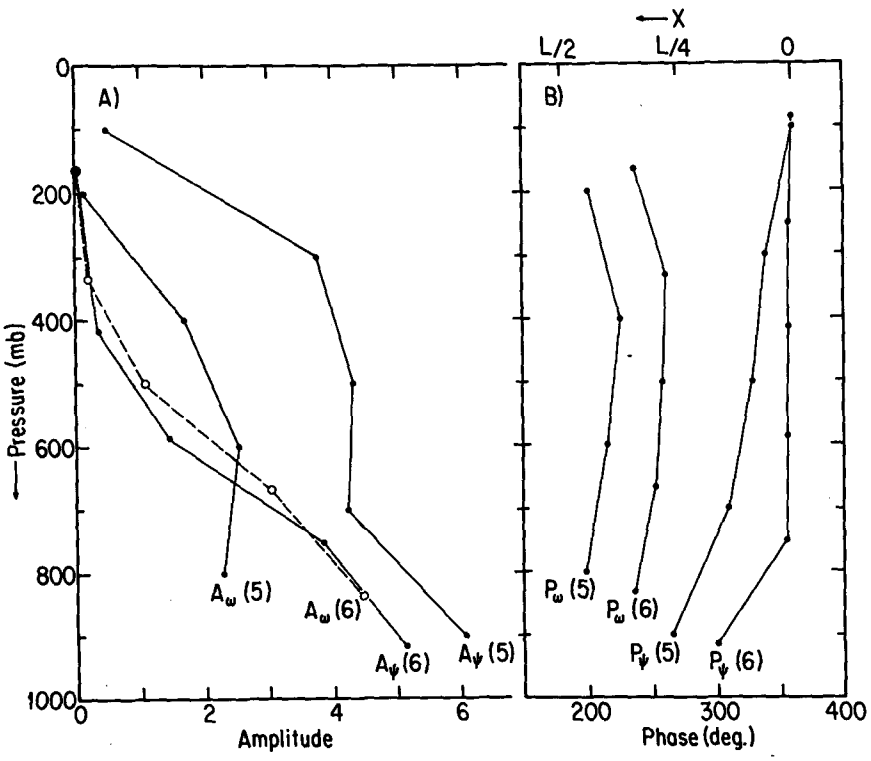

FIG. 9. As in Fig. 4 but for case b.

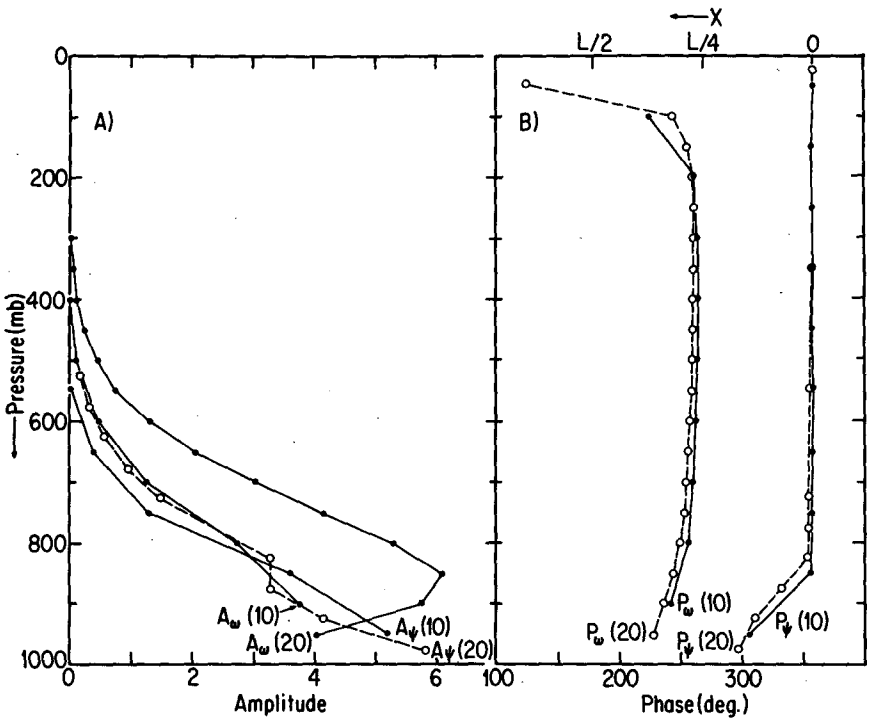

FIG. 10. As in Fig. 9 but for larger N.

Figure 12 depicts spectra for N = 3, 4, 5, 6, 9, 15 and 20. The spectra evolve rapidly as N increases from 3. By N = 9 two equal maxima have evolved. For N > 9 the maximum at the shorter wavelength subsides, leaving one major maximum around 1900 km at large N. Altogether, there are many similarities to the spectra evolution for case a, as depicted in Fig. 2. Because of the larger shear at low levels in the present case, the final WMI is much shorter. Both cases are characterized by volatile spectral details at very short wavelengths as N is varied through intermediate and larger values.

Figure 13a depicts amplitudes of streamfunction and vertical velocity as functions of N. The amplitudes of ω, as determined for N = 5 or 9, show maxima near 800 mb (by connecting the curve to zero at p = 1000). For N = 5, there is no way of knowing that maximum

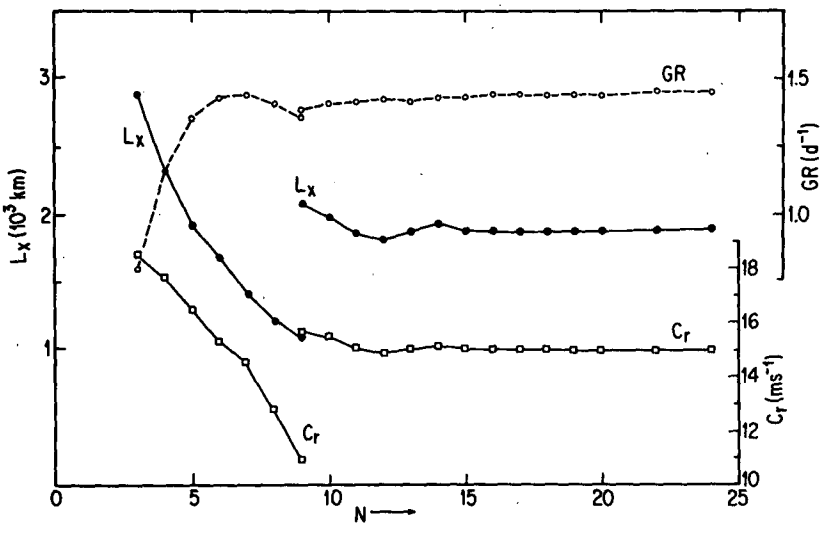

FIG. 11. As in Fig. 1 but for case c.

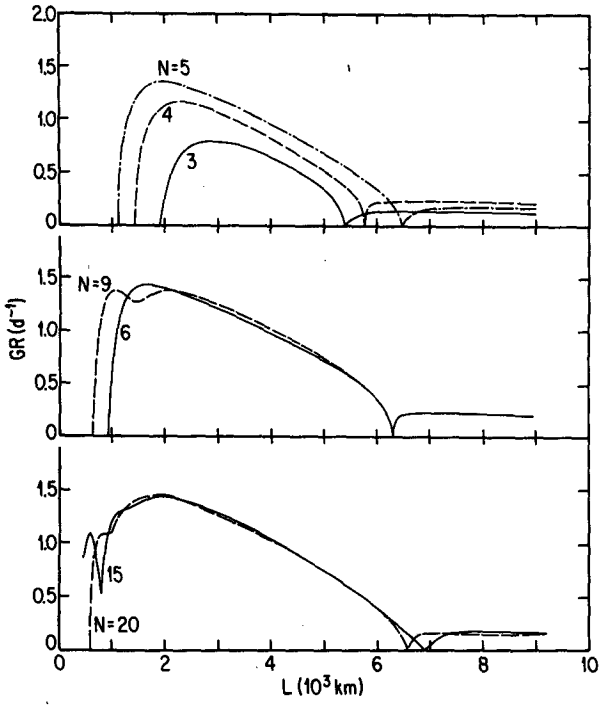

FIG. 12. As in Fig. 8 but for case c.

ω is not found substantially below 800 mb. The curve A_ω (20) clearly establishes the level of maximum ω. The curve A_ψ (20) shows a very rapid upward decrease of ψ below 800 mb, a feature that would be completely missed for $N = 5$.

Phase distributions for ψ and ω are depicted in Fig. 13b. For $N = 9$, curves are shown for $L = 1090$ and 2075 km. Both are WMI. The phase of ω relative to the phase of ψ is 20° to 30° different in the two cases.

For larger N the curves are all similar, and the rapid phase change of ω in the stratosphere is detected. This is not the case for $N = 3$.

The phases of ψ are constrained to be 360° at the uppermost level. Hence phase differences between ψ for various N are small at upper levels, but increase downward. Had phases been constrained to be the same at the lowest level, discrepancies would have increased upward.

Phase differences between ψ and ω at any level do not vary much with N for larger values of N. The difference in phase between ψ and ω is largest for $N = 3$.

d. Baroclinic instability: large shear in the upper troposphere and standard atmosphere at all levels

In this case, the plus sign in (8) is replaced by a minus sign, which puts small shear in the lower troposphere and large shear in the upper, while maintaining the same wind maximum of 30 m s^{-1} at the tropopause.

Figure 14 depicts the WMI and the corresponding growth rates and phase velocities, all as functions of N.

The two-level model senses more shear than in either of the two previous cases. The result is that these waves

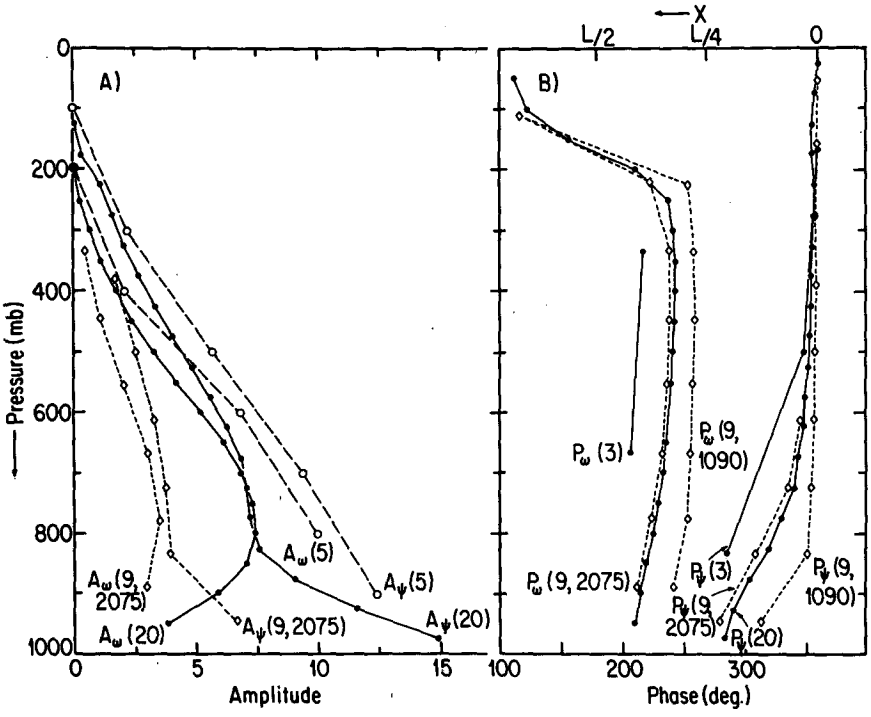

FIG. 13. As in Fig. 8 but for case c.

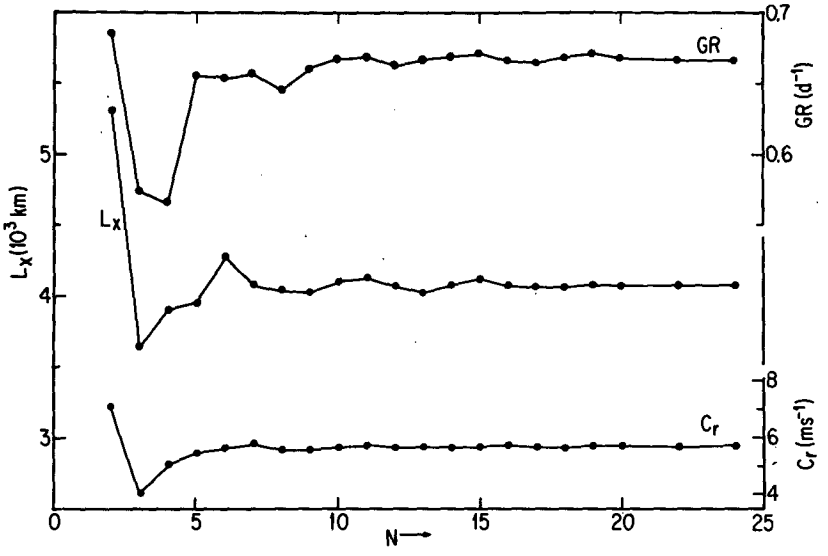

FIG. 14. As in Fig. 1 but for case d.

amplify more rapidly than for $N = 2$ in case a (linear shear). However, the WMI is similar to that in case a. As N increases from 2, the WMI decreases to a minimum at $N = 4$, then increases, resembles a damped oscillation, and finally stabilizes at slightly more than 4000 km. In case a, the final WMI is about 3400 km. The longer wavelength in the present case reflects the position of maximum shear in the upper troposphere.

As N increases from 2, the growth rate shows a minimum at $N = 4$, then increases again, finally settling down to about 0.67 d^{-1} for large N. This value is smaller than in case a and reflects the smaller shear in the lower troposphere.

The phase velocity decreases from 7 m s^{-1} for $N = 2$ to 4 m s^{-1} for $N = 3$, then increases again to about 5.7 m s^{-1} for large N.

Figure 15 depicts instability spectra for $N = 2$, 3, 4, 6, 20. The shrinking of the area under the curves and displacement toward shorter wavelengths, as N increases from 2, reflects the increased sensing of the small static stability at low levels. It is curious that the much smaller ultralongwave instability is not picked up for $N = 4$.

Unlike previous cases, the spectrum has already settled down by $N = 6$ to a shape similar to that for much larger N.

Figure 16 depicts amplitude and phase distributions for case d. Consistent with the large baroclinity in the upper troposphere, the maximum amplitude of ψ is found at the tropopause, in contrast to the lowest level in case c. The maximum of ω is now found a little above 500 mb, in contrast to the maximum at 800 mb

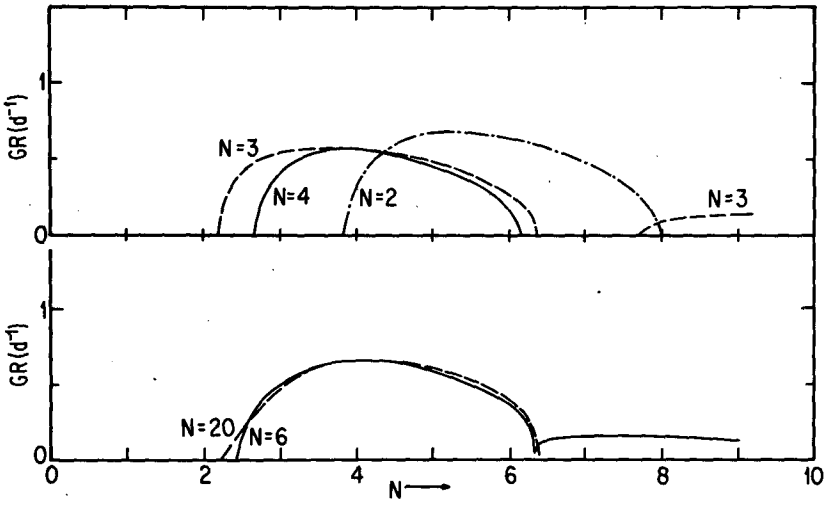

FIG. 15. As in Fig. 8 but for case d.

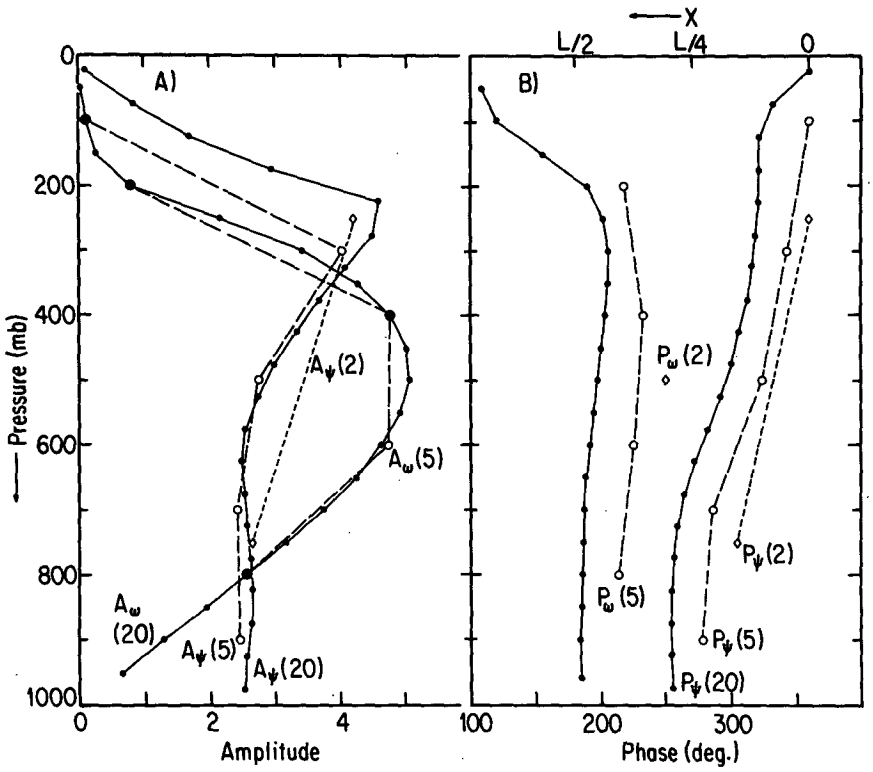

FIG. 16. As in Fig. 4 but for case d.

found in case c. The maximum amplitude of ω when $N = 5$ (and for $N = 4$, not shown) also occurs around 500 mb. The amplitude for ψ when $N = 2$ consists of only two points and misses the maximum near the tropopause.

The strong phase variations above the tropopause are mostly missed by models with small N.

e. *Barotropic instability*

The wind is described by symmetric cosine and hyperbolic secant (sech) jets having the forms

$$U = 30[1 - \cos(2\pi y/D)] \tag{9}$$

$$U = 60 \operatorname{sech}\left[\frac{8}{D}(y - D/2)\right], \tag{10}$$

where $D = 3000$ km is channel width. Both jets have a wind maximum of 60 m s^{-1} at the channel center, $y = D/2$. At $y = 0$ and D, (9) yields $U = 0$, while (10) yields $U = 2.197$ m s^{-1}. The sech jet is less sharply peaked than the Bickley one. None of the cosine, sech or Bickley jets is necessarily more representative of atmospheric jets, which on a synoptic scale show asymmetry with less anticyclonic than cyclonic shear. This is a consequence of inertial instability, which tends to wipe out any regions of negative absolute vorticity (Holton, 1979). The symmetry of the assumed jets allows the assumption of solutions symmetric about the center of the channel and increased resolution for a given matrix size.

Eigenvalues c were computed from (4) for each N as functions of wavelength for the profiles (9) and (10).

Figure 17 depicts WMI, MGR and the corresponding phase velocity c_r as functions of N. The results are qualitatively similar to those for baroclinic instability: both WMI and MGR display damped fluctuations as N is increased. However, unlike the baroclinic case, growth rate does not continue to increase with N. The explanation is apparently that the properties of the basic state (shear or static stability) near one boundary (lower) in the baroclinic case are especially influential, whereas in the barotropic case, the only effect as N is increased is the reduction of truncation error. Figure 17 also shows that low resolution may result both in overestimate and underestimate of maximum growth rate, depending on which jet profile is used.

In the case of the cosine jet, the region between the boundaries obviously contains one lateral wavelength, L_y. When $N = 3$, and for symmetric solutions, this region is divided up into six parts, each of length $d = L_y/6$. Hence, $d/L_y = 1/6$, and the finite differencing is somewhat coarse, compared with the rule of thumb that d/L_y should be of the order of 10^{-1} to keep truncation error of derivatives under 10%. However, the growth-rate spectrum is very sensitive to subtleties of the undisturbed wind distribution, and the growth rate for $N = 6$, corresponding to $d/L_y = 1/12$, is no better

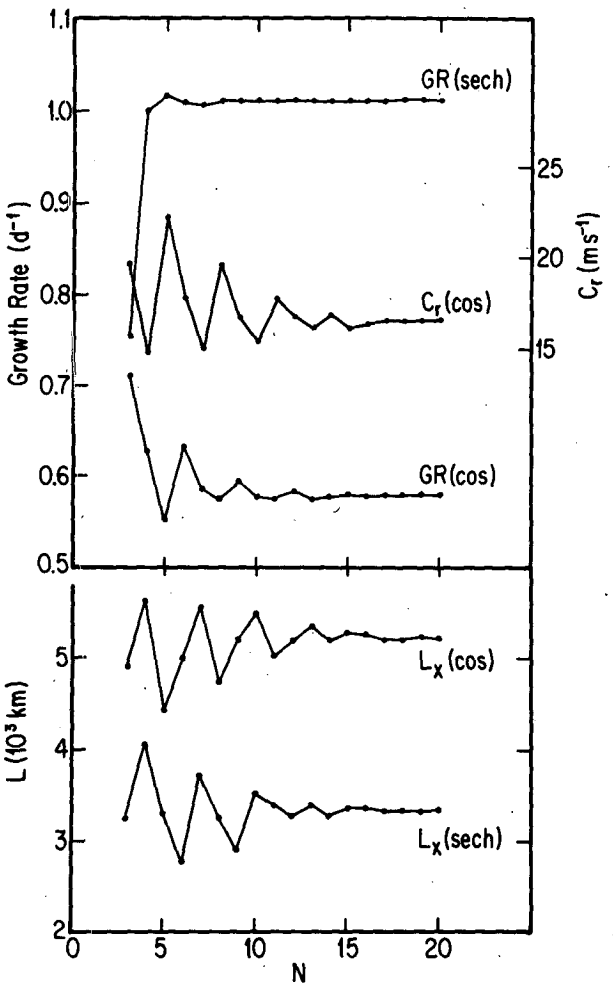

FIG. 17. Case e. Maximum growth rates (GR) and wavelengths (L_x) of maximum growth rate and corresponding phase velocity (c_r) for barotropic instability as functions of N.

than those for $N = 4$ or 5. The results indicate only that as N increases, the growth-rate spectrum eventually converges.

The phase velocity, c_r, is depicted for the cosine jet. It also displays damped oscillations. Comparisons with the L_x curve show that these are inversely related, as would be expected at long wavelengths.

For the sech jet, the damped oscillatory dependence of WMI on N is similar to that for the cosine jet. The growth rate, however, starts out being underestimated by about 25%, but rapidly approaches a constant as N is increased.

Figure 18 depicts growth-rate spectra for various N. The spectra are somewhat more sharply peaked than for baroclinic instability, a circumstance that makes an accurate prediction of wavelength of maximum instability somewhat more significant. For several values of N, both the cosine and sech jets show double maxima. For $N = 3$, the sech spectrum is separated into two distinct parts with a narrow neutral region in between. For other parameters in (10)—those that broaden the half-width of the jet, for example—the spectrum might not separate into two parts.

4. Summary and conclusions

Increasing the vertical resolution eventually leads to invariant baroclinic instability spectra at intermediate and long wavelengths. However, the improvement as N increases is not necessarily monotonic, and the addition of one or two levels, when N is small, may actually lead to worsening of computed growth rate, phase velocity, and wavelength of maximum growth rate. This is especially the case with barotropic instability, which is sensitively dependent on the distribution of $\beta - \partial^2 U/\partial y^2$. The results also suggest that the computed barotropic instability of observed atmospheric flows can be very different from the actual instability if the wind distribution is inaccurately known.

Some causes for the various overall trends of the WMI, MGR and phase velocity curves in Figs. 1, 7, 11, 14 and 17 have been identified in terms of the evolving sampling of shear and static stability as N is varied.

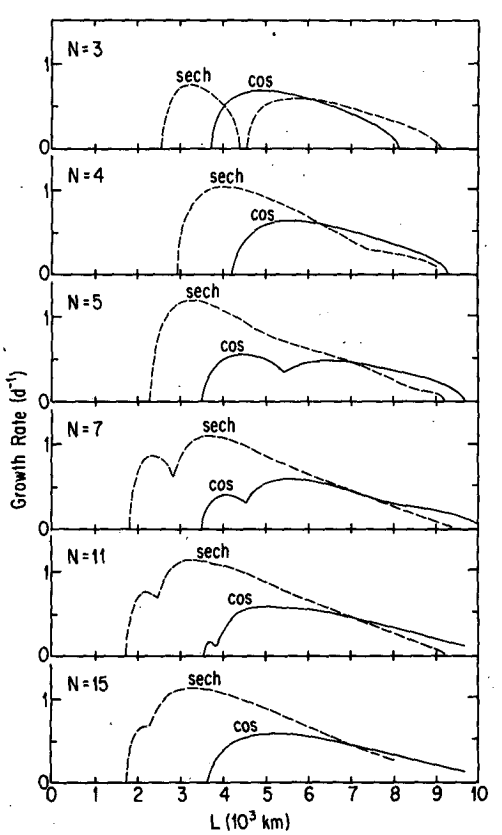

FIG. 18. Case e. Growth-rate spectra for barotropic instability as functions of wavelength for various N.

In the common baroclinic cases a, b and c (Figs. 1, 7 and 11), large N predicts much shorter waves, growing much more rapidly, and propagating much more slowly, as compared with the predictions for small N ($\leqslant 5$). When baroclinity is largely confined to the lower troposphere, the two-level model may even miss the existence of instability.

Causes for the damped oscillatory behavior of the growth rate, wavelength and phase velocity curves in cases a, c, d and e (Figs. 1, 11, 14 and 17) could not be identified. The phenomenon is perhaps related to an irregular periodicity superimposed on the decreasing truncation errors as N is increased. For example, in the case of barotropic instability, three levels occur at the same y for $N = 3$ and 6; and four levels occur at the same y for $N = 4$ and 8. The shifting proximity of grid points to inflection points may also be a factor.

Much of the oscillatory behavior in case b seems to be related to the periodic appearance of additional levels in the region of small static stability below 800 mb.

The most obvious deficiency in the structure corresponding to small N is incomplete description. For $N = 2$, vertical velocity is computed only at 500 mb, and streamfunction only at 250 and 750 mb. The phase difference between ω and ψ can therefore be estimated only at one level and change of phase of ψ with height can be determined only as a crude average over 500 mb. As N increases from 2, the development of a reasonably complete description of structure is very gradual. Fluctuations of phase difference between ψ and ω at 500 mb are of the order of 20° or 30° as N is increased from 2. Even for $N = 10$, the uncertainty in the level of maximum vertical velocity can be of the order of 100 mb if there is strong baroclinity or low static stability in the lower troposphere.

The structure may vary rapidly in the stratosphere and in the lower troposphere, as revealed by $N = 20$. These sharp variations can be largely missed for $N \leqslant 10$.

The poor performance of the two-level, quasi-geostrophic model used here reflects the application of the thermodynamic energy at the intermediate level. This deficiency may be removed by application of the quasi-geostrophic potential vorticity equation to the two levels, thereby introducing static stability at the two levels instead of the one intermediate level. The application of the boundary conditions $\omega = 0$ at $p = 0$ and 1000 mb is somewhat more difficult, requiring conditions on U and dU/dp determined by noncentered differences. The exploration of this type of N-level model goes beyond the scope of the present study, but will perhaps be the subject of a future investigation.

Simmons and Hoskins (1976) conclude that low vertical resolution leads to spuriously large growth rates at high zonal wavenumbers (N_z). The basis of this conclusion was the finding of substantial growth rate for $8 \leqslant N_z \leqslant 15$ for $N = 2$, and larger growth rates for $N = 5$ than for $N = 8$, 16 over the same range of N. These results are contrary to those found here. It is difficult to account for the discrepancies without greater familiarity with the models, as well as details of the shears and static stabilities actually used. These are now known to be crucial. The initial value technique used by them is subject to error when there exist more than one amplifying mode at the same wavenumber, a possibility in view of the eigenvalues found in the present study.

This investigation supports previous conclusions by Moen (1974), Simmons and Hoskins (1976), Staley and Gall (1977) and Satyamurty et al. (1982) that high vertical resolution improves the description of baroclinic instability at short wavelengths. However, the support is only in the sense that low vertical resolution in the quasi-geostrophic model may miss the existence of instability at wavelengths of the order of 500 to 2000 km. With high vertical resolution, narrow peaks appear in the quasi-geostrophic model within this range of wavelength and then shift to still shorter wavelengths as N increases. These peaks have been shown to appear in response to variation of N alone, in the case where static stability was always that of the standard atmosphere, and $\partial U/\partial p$ was constant. It is not obvious that the inclusion of ageostrophic effects would eliminate these peaks that appear and propagate in response to variation of N. There appears to be a need for systematic numerical experimentation with varying N in ageostrophic models, as well as in quasi-geostrophic models with differencing schemes that apply static stability at the same levels where the vorticity equation is applied.

The numerical results reported here were obtained using a Commodore-64 and a Tandy-2000. The wide range of matrix sizes used corresponded to a painfully perceptible variation of computation times. In view of the proliferation of personal computers on campus (Waldrop, 1985), the details and computation times given in the Appendix may be of interest.

Acknowledgments. The author wishes to thank E. A. Staley, who assisted with the programing, and M. Sanderson-Rae, who edited the manuscript.

APPENDIX

Eigenvalue Computation Times

The eigenvalues were computed from a BASIC program given by Shoup (1984). This program includes direct reduction of a matrix to upper Hessenberg form, followed by application of the QR algorithm as described by Martin et al. (1970). The program was not compiled.

With the Commodore-64, the total time τ to compute the elements of $\mathbf{A}$ and $\mathbf{B}$ in (4), find $\mathbf{B}^{-1}$, then find $\mathbf{M} = \mathbf{B}^{-1}\mathbf{A}$, put $\mathbf{M}$ in upper Hessenberg form, find eigenvalues by the QR algorithm, and print the results is given, approximately, for $N \geqslant 3$ by

$$\tau = 9.74 \times 10^{-3} N^{8/3}$$

where τ is in minutes. For $N = 5$, 10, 15, 20, 25, we find $\tau = 0.71$, 4.5, 13.3, 28.7, 52.0 minutes, respectively. Times for individual runs vary because of varying numbers of iterations required for convergence, etc. For $N = 25$, most values of τ lie in the range 49–55 min. For smaller N, the percentage variation of τ was similar. Most of the computation time is spent finding $\mathbf{B}^{-1}$ and eigenvalues.

With the Tandy-2000, computation time was a more complicated function of N. For $N < 5$, the Commodore-64 computed and printed the results in less time, although, with both computers, the times were less than half a minute. For $N > 15$, the times for the Tandy 2000 varied approximately as

$$\tau = 4.36 \times 10^{-3} N^{2.55}.$$

For $N = 15$, 20, 25, we find $\tau = 4.4$, 9.1, 16.0 minutes, respectively. Hence, for this range of N, the Tandy-2000 was slightly more than three times faster than the Commodore-64. It must be noted that computation times are but one relevant consideration. Machine precision is important in the computation of eigenvalues, particularly when matrix size is large and eigenvalues close together. The Tandy-2000 has a double precision of 10^{-17}, whereas the Commodore-64 is accurate to 10^{-9}. Using the same algorithm, the Tandy-2000 usually finds accurate eigenvalues where the Commodore-64 fails. For many matrices, precision is not a problem; for some matrices, it can be a serious problem.

The times required clearly do not allow instant gratification and become prohibitive for large matrix sizes. However, as noted by Waldrop, the desktop computer is more convenient and accessible than the big mainframes and supercomputers, where time has to be shared. In the present experience, the long computing times for looping through wavelength at larger N was variously spent interpreting results, doing other research, teaching, and doing none of the above.

Errors in the eigenvalues were not a significant problem for the matrices encountered here. Some comparisons were made with the eigenvalues of $\mathbf{M}^T$, and also with eigenvalues computed from a related program running on a CYBER 175 utilizing the EISPACK eigensystem package (Smith et al., 1976).

REFERENCES

Brown, J. A., 1969: A numerical investigation of hydrodynamic instability and energy conversions in the quasi-geostrophic atmosphere. Part I. *J. Atmos. Sci.*, **26**, 352–365.

Charney, J. G., and N. A. Phillips, 1953: Numerical integration of the quasi-geostrophic equations for barotropic and simple baroclinic flows. *J. Meteor.*, **10**, 71–99.

Haltiner, G. J., and R. T. Song, 1962: Dynamic instability in barotropic flow. *Tellus*, **4**, 383–393.

Hirota, I., 1968: On the dynamics of long and ultra-long waves in a baroclinic zonal current. *J. Meteor. Soc. Japan*, **46**, 234–249.

Hollingsworth, A., 1975: Baroclinic instability of a simple flow on the sphere. *Quart. J. Roy. Meteor. Soc.*, **101**, 495–528.

Holton, J. R., 1979: *An Introduction to Dynamic Meteorology.* Academic Press, 391 pp.

Lorenz, E. N., 1960: Energy and numerical weather prediction. *Tellus*, **12**, 364–373.

MacVean, M. K., 1983: The effects of horizontal diffusion on baroclinic development in a spectral model. *Quart. J. Roy. Meteor. Soc.*, **109**, 771–783.

Martin, R. S., G. Peters and J. H. Wilkinson, 1970: The QR algorithm for real Hessenberg matrices. *Numer. Math.*, **14**, 219–231.

Moen, L., 1974: A spectral model for investigation of amplifying baroclinic waves. *Tellus*, **26**, 424–443.

Phillips, N. A., 1954: Energy transformations and meridional circulations associated with simple baroclinic waves in a two-level quasi-geostrophic model. *Tellus*, **6**, 273–286.

Satyamurty, P., V. B. Rao and A. D. Moura, 1982: Subsynoptic-scale baroclinic instability. *J. Atmos. Sci.*, **39**, 1052–1061.

Shoup, T. E., 1984: *Applied Numerical Methods for the Microcomputer.* Prentice Hall, 262 pp.

Simmons, A. J., and B. J. Hoskins, 1976: Baroclinic instability on the sphere: Normal modes of the primitive and quasi-geostrophic equations. *J. Atmos. Sci.*, **34**, 1454–1477.

Simons, T. J., 1972: On the theory of atmospheric development. *Mon. Wea. Rev.*, **100**, 145–152.

Smith, B. T., J. M. Boyle, J. J. Dongarra, B. S. Garbow, Y. Ikebe, V. C. Klema and C. B. Moler, 1976: *Matrix Eigensystem Routines—Eispack Guide.* Springer-Verlag, 551 pp.

Staley, D. O., and R. L. Gall, 1977: On the wavelength of maximum baroclinic instability. *J. Atmos. Sci.*, **34**, 1679–1688.

Waldrop, M. M., 1985: Personal computers on campus. *Science*, **228**, 438–444.